processes

MDPI

Article

Unveiling the Potential of Room-Temperature Synthesis of a Mixed-Linker Zeolitic Imidazolate Framework-76 for CO_2 Capture

Asyraf Hanim Ab Rahim [1,2], Noor Fazrieyana Hamidon [1], Normawati M. Yunus [1,2,*], Mohamad Azmi Bustam [1,3], Siti Fatimah Nur Abdul Aziz [4], Khairulazhar Jumbri [1,2] and Emilia Abdulmalek [5]

[1] Centre for Research in Ionic Liquid (CORIL), Institute of Sustainable Energy and Resources (ISER), Universiti Teknologi PETRONAS, Seri Iskandar 32610, Perak, Malaysia; asyrafhanim92@gmail.com (A.H.A.R.); fazrieyana@utp.edu.my (N.F.H.); azmibustam@utp.edu.my (M.A.B.); khairulazhar.jumbri@utp.edu.my (K.J.)
[2] Department of Fundamental and Applied Sciences, Universiti Teknologi PETRONAS, Seri Iskandar 32610, Perak, Malaysia
[3] Department of Chemical Engineering, Universiti Teknologi PETRONAS, Seri Iskandar 32610, Perak, Malaysia
[4] School of Chemical Sciences, Universiti Sains Malaysia, Gelugor 11800, Penang, Malaysia; fatimahnuraa@usm.my
[5] Department of Chemistry, Faculty of Science, Universiti Putra Malaysia, Serdang 43400, Selangor, Malaysia; emilia@upm.edu.my
* Correspondence: normaw@utp.edu.my

Abstract: A room-temperature synthesis was used to prepare ZIF-76 by combining the organic linker imidazole and 5-chlorobenzimidazole, with the addition of NaOH as a modulator. The synthesis process was optimized by modifying the existing method, which includes the introduction of heating, different types of solvent, and adjustment to the reactant ratio. The synthesized MOFs were characterized to evaluate their crystallinity, textural properties and surface morphology. The result demonstrated that the introduction of heat led to the formation of ZnO whereas the replacement of DEF–DMF with methanol resulted in the production of amorphous material. Moreover, a change in precursor ratio led to the production of ZIF-76 with a low yield and surface area. Meanwhile, CO_2 adsorption was performed in a pressure range of 0–1.2 bar at 298.15 K. Notably, ZIF-76_B with a low surface area exhibited a greater CO_2 uptake capacity of 1.43 mmol/g compared to ZIF-76_A, which recorded 1.29 mmol/g. Furthermore, the isotherm and kinetic models were applied to fit the experimental CO_2 adsorption data. The analysis of the adsorption models indicated that the CO_2 adsorption was primarily governed by a monolayer formation on a homogeneous surface. Nevertheless, there was a slight diversion in terms of predicted q_m with experimental data, which could be attributed to the adsorption not yet reaching equilibrium. Additionally, the kinetic model was applied to the initial stage of adsorption in the pressure range of 0–0.24 bar. The Elovich model was found to fit better with the CO_2 uptake capacity data of ZIF-76_A and ZIF-76_B suggesting that the adsorption process may involve multiple mechanisms.

Keywords: metal–organic frameworks; zeolitic; carbon dioxide; adsorption; capture; isotherm; kinetic

check for updates

Academic Editors: Hamidreza Mahdavi and Joseph Olorunyomi

Received: 29 December 2024
Revised: 18 January 2025
Accepted: 22 January 2025
Published: 24 January 2025

Citation: Rahim, A.H.A.; Hamidon, N.F.; Yunus, N.M.; Bustam, M.A.; Aziz, S.F.N.A.; Jumbri, K.; Abdulmalek, E. Unveiling the Potential of Room-Temperature Synthesis of a Mixed-Linker Zeolitic Imidazolate Framework-76 for CO_2 Capture. *Processes* **2025**, *13*, 320. https://doi.org/10.3390/pr13020320

Copyright: © 2025 by the authors. Licensee MDPI, Basel, Switzerland. This article is an open access article distributed under the terms and conditions of the Creative Commons Attribution (CC BY) license (https://creativecommons.org/licenses/by/4.0/).

1. Introduction

Metal–organic frameworks (MOFs) are a class of promising porous materials, constructed by the interconnection of inorganic metal nodes with an organic ligand. First

introduced by Yaghi and co-workers in the 1990s, MOFs have garnered sustained interest, with the number of newly synthesized MOFs steadily increasing each year. In the meantime, a zeolitic imidazolate framework (ZIF) is a subclass of MOFs with zeolite topological-like structure [1]. Generally, ZIF-MOFs are formed by tetrahedrally coordinated transition metal cations with imidazole ligand such as 2-methylimidazole, imidazole, and 1-methylbenzimidazole. To date, ZIFs are among the extensively studied subclasses of MOFs due to their ability to alter the chemical and physical properties based on secondary building units (SBUs) [2]. ZIFs have also garnered significant attention due to their diverse applications including catalysis, sensor, gas capture, and storage [3–5]. For example, ZIF-8 has been widely utilized in gas capture with recent advancements focusing on its integration into various materials such as membranes and ionic liquids (ILs) to enhance performance [6,7]. Meanwhile, ZIF-90 has found significant applications in the biomedical field, including biosecurity, anticancer therapy, and photodynamic therapy [8].

Up to this day, numerous ZIFs have been prepared including mixed-linker ZIF-MOFs. The development of mixed-linker MOFs was proposed with the aim of improving the functionality and versatility of materials. Ahlen and co-workers utilized a series of mixed-linker ZIF-7-8s for CO_2 adsorption. The MOFs was synthesized using different ratios of benzimidazolate (bIm) and 2 methylimidazolate (mIm), producing ZIF-MOFs with different topology [9]. It was found that the CO_2 adsorption capacity of mixed-linker ZIF-7-8s at all ratios surpassed that of ZIF-8 alone, demonstrating the enhanced performance achieved through the incorporation of multiple linkers. On the other hand, ZIF-76 is a mixed-linker MOF comprised of zinc coordinated by a mixture of ligands, namely, imidazole (Im) and 5-chlorobenzimidazole (bIm), hence forming a Linde Type A (LTA) topology in a cuboctahedron structure [10]. Generally, the pore aperture and diameter of ZIF-76 are 5.4 and 12.2 Å, respectively. Furthermore, the presence of the benzimidazolate linker enhances the material's affinity towards CO_2. The benzimidazolate provides an additional binding site, thereby facilitating stronger interactions with CO_2 molecules [11]. This leads to an improvement in CO_2 adsorption capacity. Coupled with its large surface area and high thermal stability, ZIF-76 emerges as a promising material for adsorption and separation, particularly in gas capture processes.

However, initial work on the synthesis of ZIF-76 involved a solvothermal synthesis that employed polar organic solvents like dimethylformamide (DMF) and diethylformamide (DEF) [4]. The solvothermal synthesis of ZIF-76 typically involves a reaction conducted at 65 °C over an extended duration of 5 days, often resulting in a relatively low product yield which is not suitable to be applied at larger scale. Subsequently, the synthesis method for ZIF-76 was modified to enhance the product yield. An initial study by Peralta and co-workers demonstrated that the addition of sodium hydroxide (NaOH) improved the yield of ZIF-76 by 1.8 times under reaction conditions of 90 °C and a duration of 5 days [12]. In addition, current procedures of synthesizing ZIFs must deal with polymorphisms. Polymorphisms refer to the existence of different crystallographic structure resulting from different packing arrangements of its molecules in the crystal structures [13,14]. The addition of a modulator such as NaOH plays a crucial role in enhancing crystal morphology and increasing yield, especially under room-temperature synthesis conditions. In particular, Deneff et al. demonstrated the successful synthesis of ZIF-76 at room temperature using a DMF and DEF mixture in which the addition of NaOH was essential for crystal formation [15].

In this work, ZIF-76 was synthesized using a direct mixing method in which different reaction parameters including temperature, modulator, and precursor ratios were systematically explored to determine the ideal synthesis conditions. The polymorphic phenomenon of ZIF-76 was studied by examining the interaction between metal and linkers through analyzing its crystallization phases, which are influenced by the interaction of various

parameters that have the potential to impact the properties of ZIF-76. The resulting MOF was also evaluated for its physicochemical properties including crystallinity, textural properties, functional group interaction, and morphology. Additionally, the resulting ZIF-76 was tested for carbon dioxide (CO_2) adsorption in the pressure range of 0–1.2 bar. While ZIF-76 has previously been reported for CO_2 capture, detailed investigations into its adsorption isotherms and kinetics have not been performed. Hence, this work provides a comprehensive analysis of the adsorption behavior of ZIF-76 by employing both two- and three-parameter adsorption isotherm models such as Langmuir, Freundlich, Sips, and Toth, to gain a deeper insight into the gas capture mechanism. Additionally, kinetic modeling using pseudo-first-order, pseudo-second-order, and Elovich models were conducted to examine the rate-determining step of single-CO_2 adsorption.

2. Materials and Methods

2.1. Materials

All chemicals were purchased from commercial sources and were used without purification unless indicated otherwise. The CAS number, purity, and manufacturer were as follows:

Zinc nitrate hexahydrate, $Zn(NO_3)_2.6H_2O$ (10196-18-6, 99%, Sigma-Aldrich, St. Louis, MO, USA), 5-chlorobenzimidazole (4887-82-5, 96%, Sigma-Aldrich), imidazole (288-32-4, 99%, Sigma-Aldrich), N, N-dimethylformamide (68-12-2, 99.8%, Sigma-Aldrich), N,N-diethylformamide (617-84-5, 99%, Sigma-Aldrich), methanol (67-56-1, 99.9%, R&M Chemicals, Semenyih, Malaysia), and sodium hydroxide (1310-73-2, 98.5%, Merck, Singapore).

2.2. Methods

2.2.1. Synthesis of ZIF-76

As mentioned in the previous section, an initial study reported the solvothermal synthesis of ZIF-76 occurred at a temperature of 65 °C over a prolonged reaction time of 48–96 h and often resulted in a low product yield. In this work, ZIF-76 was synthesized under various operational conditions by modifying the reaction parameters including precursor ratios, type of solvent, temperature, and duration. Table 1 lists the different synthesis conditions.

Table 1. Synthesis conditions for ZIF-76.

Run	Temperature (°C)	Duration (hours)	Zn^{2+} (mmol)	n Im (mmol)	n bIm (mmol)	Solvents	n NaOH (mmol)
1	25	120	2.61	17.25	0.86	DMF–DEF (1:1 v/v)	1.95
2	25	120	0.86	17.25	0.86	DMF–DEF (1:1 v/v)	0.86
3	25	120	2.61	17.25	0.86	DMF–DEF (1:1 v/v)	0
4	25	120	0.86	17.25	0.86	DMF–DEF (1:1 v/v)	0
5	80	24	2.61	17.25	0.86	DMF–DEF (1:1 v/v)	1.95
6	25	120	2.61	17.25	0.86	methanol	1.95

Meanwhile, the optimal reaction condition was based on methods reported by Deneff and co-workers. Imidazole (17.25 mmol) and 5-chlorobenzimidazole (0.86 mmol) were added into the mixture of 9 mL N-N-dimethylformamide: N,N-diethylformamide (1:1 v/v) and stirred for 10 min. Then, $Zn(NO_3)_2{\cdot}6H_2O$ (2.61 mmol, 2.5 mL) and the NaOH solution (1.95 mmol, 2.5 M in water) were added into the linkers' solutions and stirred for 30 min. The mixture was then left out for 120 h at room temperature to react. The solid precipitates were collected by washing with dimethylformamide three times followed by re-dispersing in methanol. The solvent exchange process was repeated for 3 days in which methanol was

changed every 24 h. Subsequently, the precipitate was collected and dried in an oven at 100 °C. The resulting sample was designated as ZIF-76_A.

Subsequent syntheses utilized the same procedure by maintaining the ratio of organic linker but with different mol of $Zn(NO_3)_2 \cdot 6H_2O$ and NaOH solution (0.65 mmol, 2.5 M in water). This MOF was designated as ZIF-76_B.

2.2.2. Characterization

The powder X-ray diffraction (PXRD) patterns were obtained using the PANalytical Malvern Xpert3 Powder XRD, Malvern, United Kingdom. Diffraction data were collected from 2θ = 2–80°, at a scan rate of 0.03 min^{-1} using Cu Kα (λ = 1.540598 Å) radiation. The functional group identification of MOFs was investigated using a Fourier transform infrared spectrometer (FTIR), the Thermo-Nicolet iS5, Thermo Fisher Scientific, Waltham, Massachusets, United States. The spectra were collected in the wavenumbers ranging from 380 to 3999 cm^{-1}. The solid sample was mixed with potassium bromide (KBr) and palletized prior to functional group analysis. Gas adsorption isotherms were obtained from a TriStar II 3020 analyzer from Micromeritics, Norcross, Georgia, United States. The sample was degassed at 250 °C for 12 h to remove moisture and any adsorbed gas or molecules prior to measurement. Nitrogen adsorption–desorption isotherms were measured at 77 K. The morphology and particle size of MOFs were determined by using a transmission electron microscope (TEM) from Hitachi, Chiyoda City, Tokyo, Japan, model HT7830.

2.2.3. Single-CO_2 Adsorption Analysis

The CO_2 adsorption by MOFs was measured volumetrically using MicroActive for TriStar II Plus 2.03 adsorption equipment from Micromeritics, Norcross, GA, USA. The adsorption of CO_2 was measured at 298.15 K in the pressure ranging from 0 to 1 bar. About 0.20 g of sample was loaded into the cell. Prior to the analysis, the sample was activated at 250 °C for 12 h. After degassing was complete, the sample weight was recorded again before proceeding with the measurement.

2.2.4. Isotherm Modeling of CO_2 Adsorption by MOFs

In general, an adsorption isotherm describes the relationship between the amount of CO_2 adsorbed and the pressure (or concentration) at a constant temperature. It is useful for describing the distribution of adsorbate molecules and adsorption capacity of a solid adsorbent. Since decades ago, many adsorption isotherm models have been developed comprised of two and three adsorption isotherms. In this work, the experimental data on the CO_2 adsorption isotherm were fitted into two- and three-parameter adsorption isotherms, namely, Langmuir, Freundlich, Temkin, Redlich–Peterson, Sips, and Toth.

- Langmuir isotherm

The Langmuir isotherm illustrates the monolayer adsorption occurring at a homogenous surface of solid adsorbent. This model assumes one active site can adsorb only one adsorbate molecule of adsorbent with constant heat. The experimental data were fitted into Equation (1) as follows:

$$q_e = \frac{q_m K_L P}{1 + K_L P} \quad (1)$$

where q_e, q_m, and K_L are the amount of equilibrium uptake (mmol/g), maximum monolayer adsorption capacity of the adsorbent (mmol/g), and equilibrium constant ($mbar^{-1}$), respectively.

- Freundlich isotherm

The Freundlich isotherm is not limited to monolayer adsorption. Unlike the Langmuir isotherm, the Freundlich isotherm describes the non-ideal, reversible process of mono- and multilayer adsorption on a heterogenous surface. This adsorption isotherm also assumes the adsorption enthalpy exponentially decreases as the number of available adsorption sites decreases. The data of CO_2 adsorption were fitted in the following Equation (2):

$$q_e = K_f P^{\frac{1}{n}} \tag{2}$$

in which K_f and 1/n represent the adsorption capacity (mmol/g), and 1/n is the intensity of adsorbent, respectively.

- Temkin isotherm

The Temkin adsorption isotherm is based on the assumption that the heat of adsorption of all molecules in the layer falls linearly instead of exponentially with the coverage due to adsorbent–adsorbate interactions. Adsorption is also described as having a uniform distribution of binding energies. The Temkin isotherm is written as Equation (3):

$$q_e = B \ln(AP) \tag{3}$$

where B is the maximum binding energy, and A is the equilibrium binding constant.

Apart from two-parameter adsorption isotherms, the experimental data of CO_2 adsorption by MOFs were also fitted into three-parameter adsorption isotherms.

- Redlich–Peterson isotherm

The Redlich–Peterson isotherm is known as a hybrid isotherm as it features a combination of Langmuir and Freundlich isotherms. It comprises three parameters and can be used to represent adsorption equilibrium over a wide range of concentration either in a heterogenous or homogenous system. This is due to the presence of the linear-dependence concentration in the numerator and the exponential function in the denominator. The equation of the Redlich–Peterson isotherm is written as Equation (4):

$$q_e = \frac{KP}{1 + aP^g} \tag{4}$$

where K is the equilibrium constant, a is the RP parameter, and g is an exponential factor.

- Sips isotherm

The Sips isotherm is presented as Equation (5):

$$q_e = \frac{q_m (bP)^n}{1 + bP^n} \tag{5}$$

in which b, q_m, and n are the equilibrium constant, maximum adsorption capacity (mmol/g), and Sips heterogeneity constant, respectively. The Sips isotherm is formed by a combination of Langmuir and Freundlich expressions to predict a heterogenous adsorption system. At low adsorbate concentration, the model reduces to the Freundlich isotherm. Meanwhile, the model is transformed into the Langmuir isotherm at high adsorbate concentrations. In general, the parameters in Sips's equation can be affected by the change in reaction conditions such as pH, temperature, and concentration.

- Toth isotherm

The Toth isotherm was designed to improve the Langmuir isotherm. The Toth isotherm model describes heterogeneous adsorption systems and assumes an asymmetrical quasi-

Gaussian energy distribution with a widened left-hand side, i.e., most sites have an adsorption energy lower than the mean value. It can be represented by the following Equation (6):

$$q_e = \frac{q_m bP}{1 + (bP^t)^{\frac{1}{t}}} \quad (6)$$

where b and t are the surface affinity and surface heterogenicity parameter, respectively.

2.2.5. Kinetic Modeling of CO_2 Adsorption by MOFs

Understanding the adsorption kinetic is crucial for designing and quantifying the adsorption mechanism. Several kinetic models have been used to describe the CO_2 capture process such as pseudo-first-order, pseudo-second-order, and Elovich models as shown in Equations (7)–(9) below:

$$q = q_s\left(1 - exp^{-k_1 t}\right) \quad (7)$$

$$q = q_s\left(1 - \frac{1}{1 + q_s k_2 t}\right) \quad (8)$$

$$q_t = \frac{1}{\beta}\ln(\alpha\beta t + 1) \quad (9)$$

where q_s and q are the CO_2 adsorption uptake (mmol/g) at equilibrium at t (min). Meanwhile, k_1 and k_2 are the rate constant for each corresponding model. For the Elovich model, α and β are the initial adsorption rate and desorption constant, respectively. Meanwhile, q_t is the amount adsorbed at time t.

3. Results and Discussion

3.1. XRD Analysis

The yields of ZIF-76 synthesis for each run are listed in Table S1. The presence of modulators in MOF synthesis is crucial as it significantly influences the growth and nucleation of MOFs. A study by Deneff indicates that the addition of modulators is required for MOF synthesis at room temperature [15]. The interaction of modulators with metal ions may result in the enhancement of the particle size, morphology, and overall yield of MOFs [16]. To evaluate the effect of the modulator, the synthesis was carried out both in the presence (Run 1) and absence (Run 3) of NaOH, which acted as the modulator. Both reactions were performed using a DMF–DEF solvent mixture in a 1:1 (v/v) ratio at room temperature. The absence of NaOH resulted in a significantly lower product yield with a reduction of over 98%.

Apart from that, the yield of ZIF-76 appeared to be dependent upon the interaction between the solvents and the precursors, which subsequently affected the crystallinity of the resulting crystals. To determine the role of the solvent, the XRD pattern of samples from Run 1 and Run 6 was analyzed. Interestingly, the yield of ZIF-76 synthesized in methanol (Run 6) was higher than that obtained using a DMF–DEF (1:1 v/v) solvent mixture as presented in Table S1 of Supplementary Information. Nevertheless, as shown in Figure 1a, the XRD pattern of ZIF-76_{MeOH} indicated the presence of a broad hump signifying the amorphous phase of the material. This could also be due to a poorly ordered crystal structure. Despite the higher yield achieved when methanol was used as the reaction solvent, it appeared that methanol did not provide favorable conditions for crystallization thus resulting in a material with varying degrees of crystallinity. On the contrary, the analysis on the diffractogram of ZIF-76_A revealed sharp, well-defined peaks closely matching those previously reported for ZIF-76 as well as the simulated XRD pattern, thereby confirming the successful synthesis of the material [17]. Notable characterization

peaks were observed at 2θ = 5.6, 6.8, 8.8, 9.7, 11.1, 11.6, 12.3, and 13.1° as shown in Figure 1b. These patterns of ZIF-76 suggested a structural resemblance to the typical LTA structure where each Zn^{2+} ion was tetrahedrally coordinated to three imidazolate linkers and one 5-chlorobenzimidazolate linker.

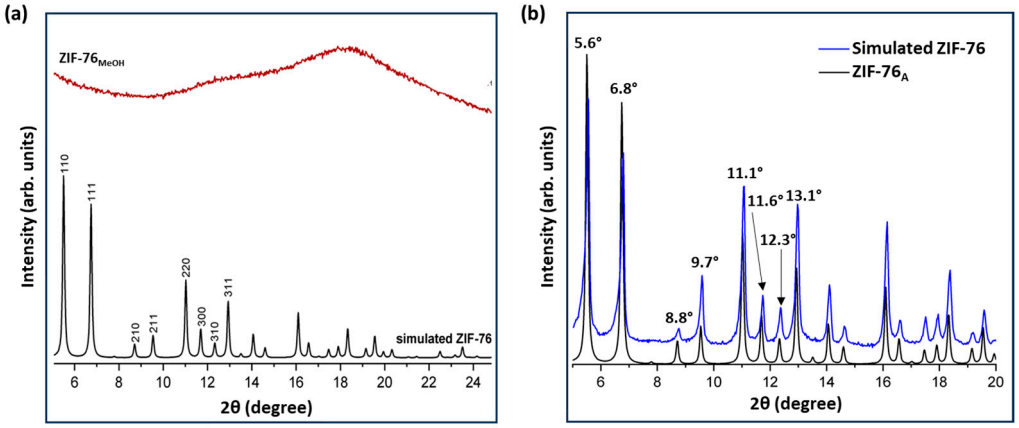

Figure 1. XRD of (**a**) ZIF-76_{MeOH} (Run 6) and (**b**) ZIF-76_A (Run 1).

To investigate the effect of temperature on the yield improvement of ZIF-76, the reaction was conducted under the same conditions as Run 1 but with heating at 80 °C. Within 24 h, the formation of a white precipitate was observed. The results revealed a significant difference in yield with ZIF-$76A_R$ showing an approximately 80% reduction in yield compared to ZIF-76_A. In addition, the PXRD analysis, as shown in Figure 2, indicates that ZIF-$76A_R$ primarily consisted of zinc oxide (ZnO) along with some unidentified phases and weak diffraction peaks compared to the simulated pattern of ZIF-76.

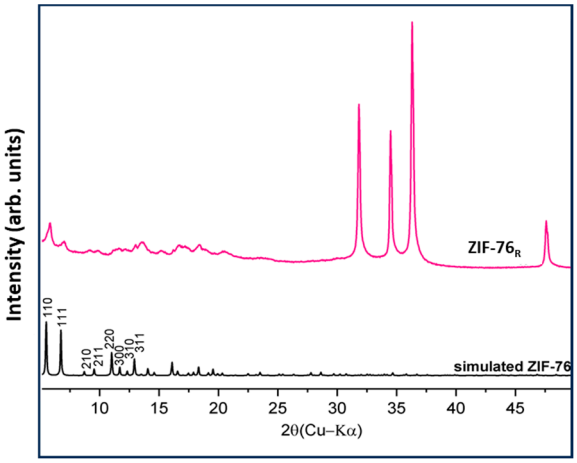

Figure 2. XRD of simulated XRD and ZIF-76_R (Run 5).

Furthermore, a study was conducted to investigate the effect of the precursor ratio by introducing different concentrations of $Zn(NO_3)_2{\cdot}6H_2O$ and NaOH while maintaining the concentration of linkers as shown in Run 2. The product from Run 2 was named ZIF-76_B. Figure 3 illustrates the XRD pattern of ZIF-76_A and ZIF-76_B along with the simulated pattern. Apart from a slight reduction in yield as shown in Table S1 of Supplementary Information, ZIF-76_B exhibited broader diffraction peaks compared to ZIF-76_A despite displaying a prominent peak characteristic of ZIF-76. The broader diffraction patterns suggested a lower crystallinity and a worse-ordered crystal structure of ZIF-76_B compared to ZIF-76_A. In terms of polymorphism, the close similarity of XRD patterns of both ZIF-76_A and ZIF-76_B with the simulated pattern suggested the absence of polymorphism. This can

be attributed to the incorporation of NaOH, which acted as modulator that facilitated linker deprotonation and prevented the formation of polymorphic structures.

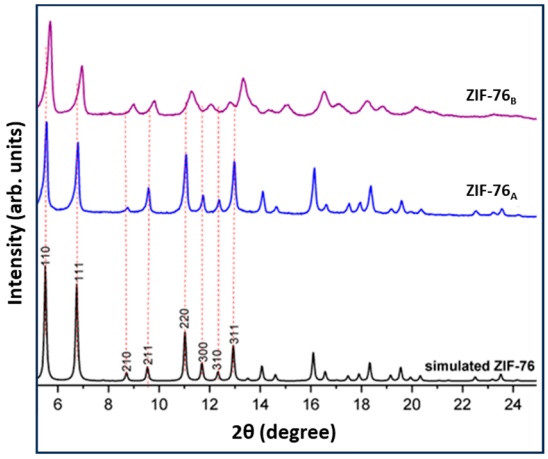

Figure 3. XRD of simulated ZIF-76, ZIF-76$_A$ (Run 1), and ZIF-76$_B$ (Run 2).

3.2. Functional Group Analysis

The synthesis of ZIF-76 resulted in the appearance of new peaks and noticeable peak shifts. For instance, the peak representing C-Cl of the halo compound shifted from 850 cm^{-1} in 5-chlorobenzimidazole, as shown in Figure S1 of Supplementary Information, to 851 and 840 cm^{-1} in the ZIF-76 spectra. Meanwhile, the FTIR spectra of ZIF-76$_A$ and ZIF-76$_B$ in Figure 4 confirmed the formation of MOFs. Overall, both samples exhibited comparable spectra, with no significant differences observed between them. Several prominent absorption bands were identified, indicating the structural similarity of the two materials. The in situ synthesis in this work utilized aqueous NaOH to promote the coordination of imidazolate-based linkers and metal ions, leading to the formation of ZIF-76 crystals. For example, ZIFs are typically characterized by the presence of prominent peaks at 808–803 cm^{-1}, which are associated with strong H-bonding within the framework. These features arise due to enhanced nucleation and coordination facilitated by the addition of NaOH as a modulator. On the other hand, the stretching vibration of Zn-N can be identified by the presence of a peak at 427–426 cm^{-1}.

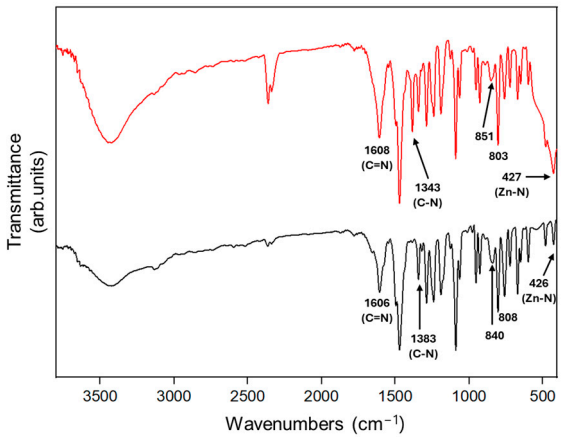

Figure 4. FTIR spectra of ZIF-76$_A$ (Run 1) and ZIF-76$_B$ (Run 2).

3.3. Textural Properties

ZIF-76$_A$ and ZIF-76$_B$ were further analyzed using the N_2 adsorption isotherm, and the resulting curves are presented in Figure 5. Both samples demonstrated a Type I N_2 adsorption–desorption isotherm, based on the IUPAC classification. This indicated the

microporous characteristic of the materials. In general, Type I is marked by a rapid intake of N_2 at very low relative pressures ($p/p_o < 0.3$), which occurs due to multidirectional interactions between the pore walls and adsorbate [18]. Meanwhile, the hysteresis loop observed can be caused by the capillary condensation [19]. ZIF-76_A exhibited higher N_2 adsorption than ZIF-76_B. These phenomena were further confirmed by the increase in volume of N_2 adsorbed at low relative pressures (at $p/p_o < 0.025$).

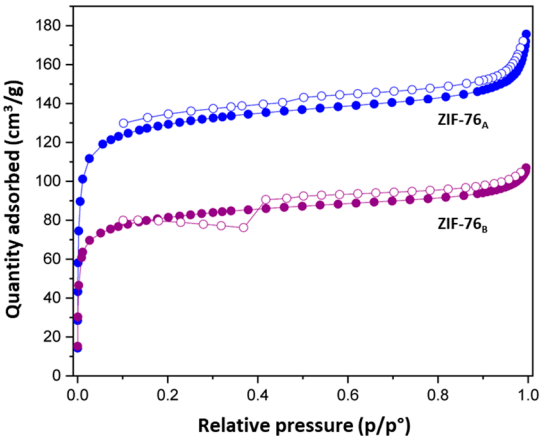

Figure 5. BET surface area curves of ZIF-76_A and ZIF-76_B.

Moreover, Table 2 presents the total surface area and pore volume of both samples. The BET surface area of ZIF-76_A was 407 m^2/g, almost two times higher than that of ZIF-76_B. The reduction in the amount of $Zn(NO_3)_2 \cdot 6H_2O$ caused a stoichiometry imbalance reaction in the synthesis of ZIF-76_B. This led to the presence of excess linkers that possibly interfered with the crystal growth thereby reducing the surface area observed in ZIF-76_B.

Table 2. The textural properties of ZIF-76_A and ZIF-76_B.

Sample	Surface Area$_{BET}$ (m^2/g)	Surface Area$_{Langmuir}$ (m^2/g)	Pore Volume (cm^3/g)
ZIF-76_A	407	589	0.26
ZIF-76_B	258	374	0.16

3.4. Morphology

The particle size and morphology of both ZIF-76_A and ZIF-76_B were studied using TEM, as shown in Figure 6. The images revealed that ZIF-76_A exhibited consistent hexagonal and cubic shapes with a uniform particle-size distribution as can be observed in Figure 6. The particle size of ZIF-76_A was determined to average 631 nm, based on the analysis of 103 particles, which was larger than previously reported values [15]. On the other hand, ZIF-76_B was found to exhibit a mixture of shapes including hexagons, needle-like structures, cubes, and spheres, as shown in Figure S2. Figure 6c,d displays the irregular formation of hexagonal structures in ZIF-76_B, in contrast to the well-defined and perfect shapes exhibited by ZIF-76_A. This observation suggests a retardation in the particle formation process of ZIF-76_B, likely caused by the presence of excess linkers. The excess linkers may hinder the uniform formation of MOF particles, resulting in the diverse morphologies observed under TEM. An off-stoichiometric ration can disrupt the balanced coordination environment that is required for uniform particle growth which in turn leads to irregularities in morphology and particle size. Due to inconsistencies in the shape of ZIF-76_B, the particle size distribution was not provided. The observed variation in the shape and particle-size distribution of ZIF-76_B could be affected by the changes in precursor ratio.

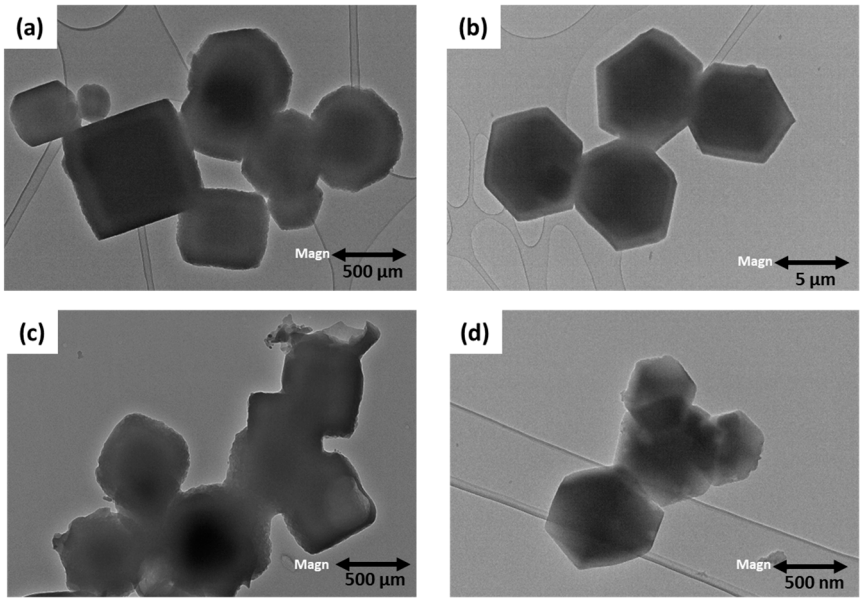

Figure 6. TEM images reveal the well-defined (**a**) cubic and (**b**) hexagonal shapes of ZIF-76_A in contrast to the irregular crystal formations observed in ZIF-76_B as shown in (**c**,**d**).

3.5. CO_2 Adsorption by ZIF-76

In this work, the single-CO_2 adsorption by ZIF-76 was conducted at a temperature of 298.15 K in the pressure range of 0–1.2 bar. For the CO_2 adsorption analysis, the study was conducted for ZIF-76_A and ZIF-76_B due to their promising yields. Figure 7 illustrates the CO_2 adsorption–desorption isotherms of both ZIF-76_A and ZIF-76_B. Overall, the CO_2 uptake capacity increased with increasing pressure. Both samples displayed a similar linear adsorption trend indicating monolayer adsorption behavior and that the maximum adsorption capacity of the materials had not yet been reached. Theoretically, gas adsorption in solid porous materials is highly dependent on the total surface area. However, the analysis of the experimental adsorption data revealed an interesting outcome in which ZIF-76_B, despite having a lower surface area than ZIF-76_A, exhibited higher CO_2 uptake. Specifically, the CO_2 uptake increased from 1.29 mmol/g for ZIF-76_A to 1.43 mmol/g for ZIF-76_B at 1 bar, 298.15 K. Altering the precursor ratio may lead to conditions known as framework defect. Defect in MOFs could lead to the presence of additional active site for the adsorption of gas molecules [20]. This led to the enhancement in the CO_2 uptake capacity of ZIF-76_B.

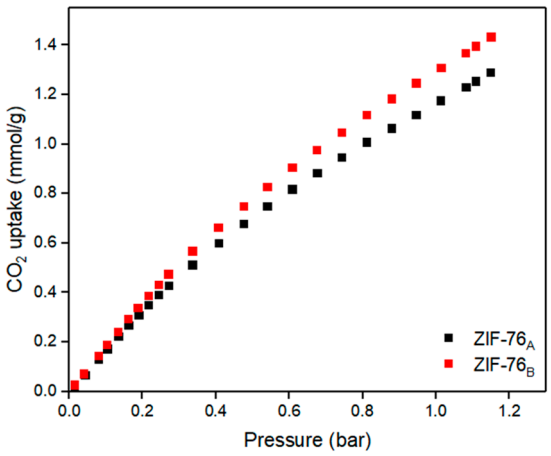

Figure 7. Single-CO_2 adsorption isotherm of ZIF-76_A and ZIF-76_B at 298.15 K under pressure ranging from 0–1 bar.

Interestingly, the CO_2 uptake recorded by ZIF-76_A and ZIF-76_B was comparable to value previously reported for ZIF-8, despite having a lower surface area. For instance, at 1 bar, the single ligand ZIF-8 exhibited a CO_2 uptake capacity of ~0.82 mmol/g while ZIF-76_A and ZIF-76_B recorded capacities of 1.29 mmol/g and 1.43 mmol/g, respectively [21]. It is anticipated that the CO_2 uptake will increase further with the application of higher pressure. The comparable CO_2 uptake by both ZIF-76 and ZIF-8 can be attributed to the presence of the mixed linker. This is consistent with previous findings by Gu et al., who demonstrated that incorporating mixed linkers of fumarate and formate led to new MOF structures and effectively enhanced the CO_2 uptake capacity [22]. In comparison, Švegovec and co-workers also investigated CO_2 capture using ZIF-76 prepared via the room-temperature synthesis procedure [23]. Their ZIF-76, which exhibited a surface area of 827 m^2/g, achieved a CO_2 uptake of 0.94 mmol/g CO_2 at 303.15 K under pressure of up to 760 torr before vitrification. While the surface area of their ZIF-76 was significantly higher than that reported in this study, the CO_2 uptake performance remains relatively comparable. This suggests the influence of additional factors beyond surface area such as the presence of active sites and the potential effect of moisture in the gas capture process. In the meantime, the desorption curve of CO_2 for both samples are presented in Figure S3 in Supplementary Information. The desorption of ZIF-76_A and ZIF-76_B is close to overlapping with the adsorption curve, indicating the adsorption process of CO_2 is reversible.

3.6. Adsorption Isotherm and Kinetic Study

Adsorption isotherm models play a crucial role in understanding the interaction between adsorbent and adsorbate [24]. Through an adsorption isotherm model, the adsorption behavior, the affinity of adsorbate towards the surface of adsorbent, and characteristics of material [25] provide valuable insights for designing optimized strategies to enhance material performance, particularly for potential applications at an industrial scale. In this work, the experimental CO_2 uptake data for both samples were analyzed using three two-parameter adsorption isotherm models, Langmuir, Freundlich, and Temkin isotherms. Additionally, three three-parameter adsorption isotherm models were applied, including the Redlich–Peterson, Sips, and Toth isotherms.

Based on the coefficient value (R^2) shown in Table 3, it was revealed that the Langmuir and Freundlich models provided the best fit for the experimental data with $R^2 > 0.99$. In contrast, the Temkin model showed an R^2 value of 0.8569–0.8620 indicating it may not be suitable to describe the adsorption process of ZIF-76_A and ZIF-76_B. The K_L value of the Langmuir isotherm can be used to evaluate the affinity of CO_2 towards the surface of MOFs. Based on Table 3, the K_L of ZIF-76_A and ZIF-76_B were 0.5261 and 0.5139, respectively. The value of $K_L < 1$ suggests that the CO_2 adsorption by both ZIF-76_A and ZIF-76_B had not yet reached the maximum adsorption capacity. This result aligns with the experimental data presented in the previous section, where the CO_2 uptake increased with rising pressure without indicating the attainment of equilibrium. A study by Ullah et al. also reported a similar low K_L value in their study related to CO_2 adsorption by UMCM-1, which the authors attributed to the incomplete coverage of adsorbate molecules on the surface of the adsorbent [26]. They concluded that increasing the pressure was necessary to achieve equilibrium under such conditions. Apart from that, the maximum adsorption capacity of the materials (q_m), as estimated by the Langmuir model, showed that ZIF-76_B exhibited a higher CO_2 uptake compared to ZIF-76_A.

Similarly, the K_f of the Freundlich isotherm, which also reflects the maximum adsorption capacity, followed the same trend as that of the Langmuir model and the experimental data. This further supported the higher CO_2 uptake observed for ZIF-76_B. Meanwhile, n in the Freundlich isotherm is the empirical constant describing the heterogenicity of

adsorbent surface. Based on Table 4, the n values of all samples fell between 1 and 10, suggesting a favorable adsorption [27]. According to Rahangdale and Kumar, the adsorption energies, namely, B ln(A) and bT = RT/B, must fall within the range of 8–16 kJ/mol and exceed 80 kJ/mol, respectively, to be indicative of chemisorption [28]. However, the calculated adsorption energies presented in Table 3 were not in the stated range, therefore signifying that the CO_2 adsorption in the MOFs studied may be primarily governed by a physisorption mechanism. Furthermore, the positive value of B in the Temkin isotherm demonstrated that the CO_2 adsorption involved an exothermic reaction. The fitting curves of the two-parameter isotherms are presented in Figure 8.

Table 3. Langmuir, Freundlich, and Temkin fitting parameters of CO_2 adsorption at 298 K.

Samples	Langmuir			Freundlich			Temkin				
	R^2	q_m (mmol/g)	K_L	R^2	K_f	n	R^2	A	B	B ln(A)	bT
ZIF-76$_A$	0.9998	3.3925	0.5261	0.9980	1.1746	1.2841	0.8620	20.7550	0.3397	1.0302	7.2974
ZIF-76$_B$	0.9998	3.8294	0.5139	0.9983	1.3051	1.2799	0.8569	21.3045	0.3730	1.1419	6.6459

Table 4. Redlich–Peterson, Sips, and Toth fitting parameters of CO_2 adsorption at 298 K.

Samples	Redlich–Peterson				Sips				Toth			
	R^2	K	a	g	R^2	q_m (mmol/g)	b	n	R^2	q_m (mmol/g)	b	t
ZIF-76$_A$	0.9999	1.8600	0.5903	0.8829	0.9999	3.5166	0.4832	0.9816	0.9999	2.9832	0.5504	0.8828
ZIF-76$_B$	0.9999	2.0936	0.6104	0.8329	0.9999	4.1341	0.4310	0.9639	0.9999	3.1539	0.5528	0.8328

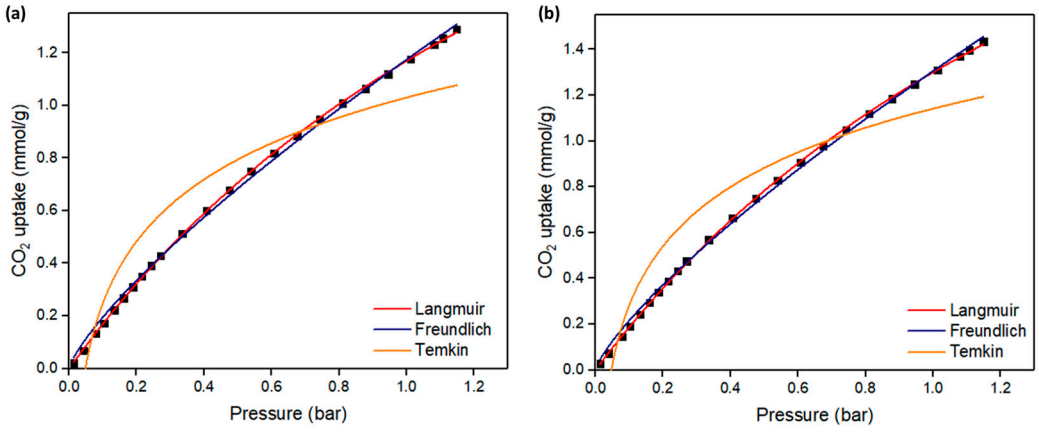

Figure 8. Two-parameter adsorption isotherm models fitting (**a**) ZIF-76$_A$ and (**b**) ZIF-76$_B$.

The data of the fit of three-parameter adsorption isotherms are tabulated in Table 4 and illustrated in Figure 9. Judging from R^2 = 0.9999, the result demonstrated that the experimental CO_2 adsorption displayed a good fitting with all adsorption isotherm models. The higher R^2 values of the Redlich–Peterson, Sips, and Toth adsorption isotherms signified the improved accuracy of these models in representing adsorption capacity compared to the previously discussed two-parameter models. The g value in the Redlich–Peterson model represents an exponential constant ranging between zero and one. In this study, the g values for both samples approached one, suggesting that the adsorption behavior closely resembled that of the Langmuir model [29]. This suggests that CO_2 adsorption in both MOFs is primarily governed by monolayer adsorption on a homogeneous surface. Meanwhile, regarding the Sips and Toth models, the magnitude of n and t were found

to be less than one, indicating a favorable adsorption. Figure 9 shows the plot of the Redlich–Peterson, Sips, and Toth adsorption for Zif-76$_A$ and ZIF-76$_B$.

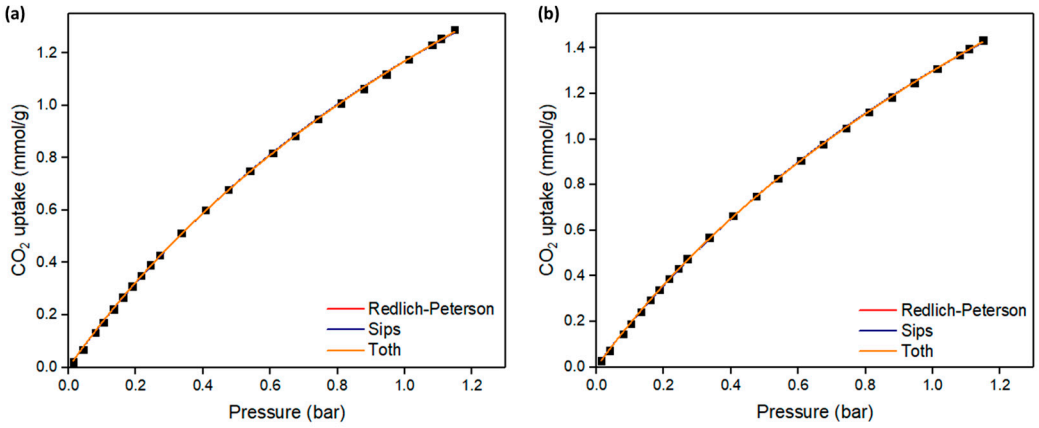

Figure 9. Three-parameter adsorption isotherm models fitting (**a**) ZIF-76$_A$ and (**b**) ZIF-76$_B$.

Generally, adsorption kinetic involves the study of the adsorbent amount as a function of time in which it provides an insight related to reaction rate and the sorption mechanism [30]. The plot contains the amount of adsorbent adsorbed as a function of time variation. In this work, both ZIF-76$_A$ and ZIF-76$_B$ gave S-shaped curves when plotting the whole adsorption process. The S-shape adsorption occurred due to the presence of two opposite mechanisms and the possibility of cooperative adsorption [31]. Hence, only the data from the initial stage of adsorption were used for kinetic modeling, as this phase is typically dominated by surface reactions. This approach allowed the kinetic models to accurately describe the interaction mechanisms without interference from later processes where the adsorption rate slows as it approaches saturation, thereby reducing the reliability of the kinetic analysis. The kinetic plot is illustrated in Figure 10 and the fitting parameters of the experimental data are given in Table 5. The initial stage of CO_2 adsorption for both MOFs was well fitted to the pseudo-first-order and pseudo-second-order models, as indicated by the R^2 values close to one. However, the low-rate constant values for both models suggested a slow adsorption process. Furthermore, the slight deviation observed in the q_e values between the experimental data and the predicted values from both models could be attributed to incomplete CO_2 adsorption during the experimental timeframe.

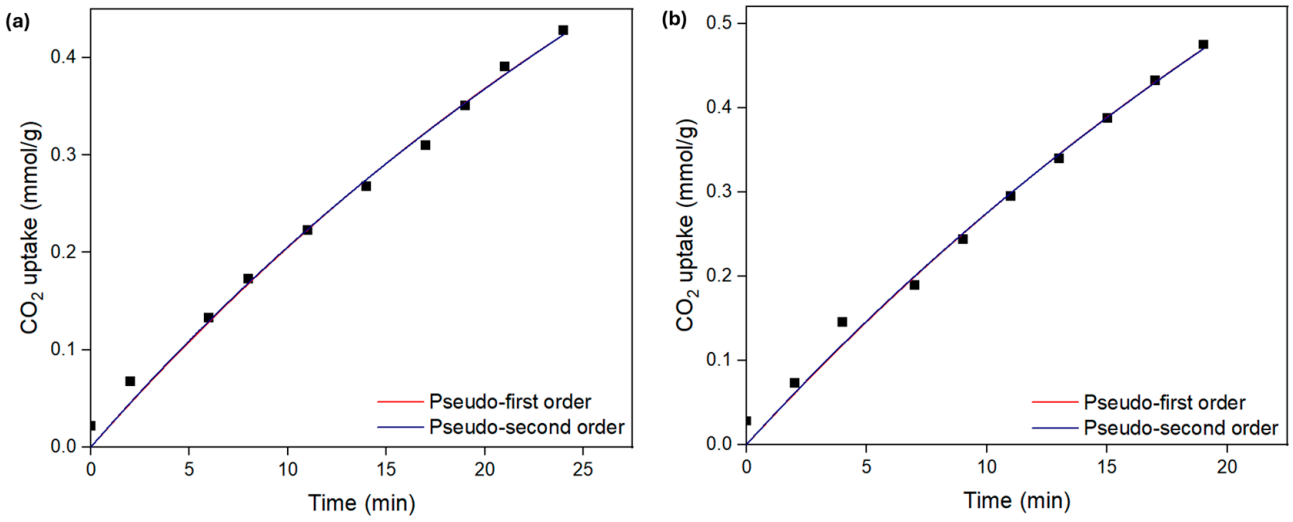

Figure 10. Pseudo-first- and pseudo-second-order models fitting (**a**) ZIF-76$_A$ and (**b**) ZIF-76$_B$ for the initial stage of CO_2 adsorption at 298.15 K.

Table 5. Fitting result of kinetic model for ZIF-76_A and ZIF-76_B for CO_2 adsorption at 298.15 K.

Samples	Pseudo-First Order			Pseudo-Second Order			Elovich		
	R^2	q_e (mmol/g)	k_1 (1/min)	R^2	q_e (mmol/g)	k_2 (mg/g.min)	R_2	α (mmol/g.min)	β (g/mmol)
ZIF-76_A	0.9922	0.9995	0.0230	0.9924	1.7455	0.0077	0.9927	0.0237	1.3294
ZIF-76_B	0.9910	1.2461	0.0249	0.9911	2.2080	0.0065	0.9913	0.0319	1.0339

Hence, we then applied an Elovich model as it has been found to be usable for a slow adsorption process. Unlike the pseudo-first- and pseudo-second-order models, the Elovich model does not assume equilibrium between adsorbate and adsorbent, hence making it suitable for analyzing the experimental data in this study that did not reach equilibrium within the experimental timeframe. The R^2 and parameter values are presented in Table 5 and the fitting graph is illustrated in Figure 11. The Elovich model with the R^2 values of 0.9927 and 0.9913 for ZIF-76_A andZIF-76_B, respectively, showed the best adjustment to the experimental data compared to the pseudo-first- and pseudo-second-order models. In addition, the value of β was greater than α, indicating a slow adsorption process and higher desorption rate.

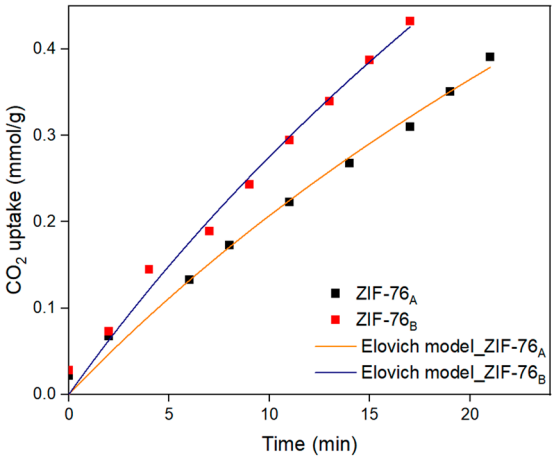

Figure 11. Elovich model fitting of ZIF-76_A and ZIF-76_B for the initial stage of CO_2 adsorption at 298.15 K.

4. Conclusions

This study reported the synthesis of a mixed-linker MOF, ZIF-76, via a direct mixing method in the presence of NaOH as a modulator to enhance crystal formation. The synthesis approach was further modified to obtain ideal synthesis conditions. Nevertheless, the TEM analysis revealed the changes in the metal–organic linker ratio resulted in the non-uniform crystal shape of ZIF-76_B. Apart from that, the textural properties evaluated through a BET analysis showed a reduction in surface area and pore volume compared to ZIF-76_A synthesized with the original metal–organic linker ratio. Meanwhile, the absence of polymorphism in the synthesized ZIF-76_A and ZIF-76_B provides an advantage for industrial-scale synthesis, as it ensures uniformity and reproducibility of their properties. On the other hand, interestingly, CO_2 adsorption experiments conducted at 298.15 K revealed that ZIF-76_B, despite having a low surface area, exhibited a higher gas uptake capacity. However, the adsorption process did not reach equilibrium within the measured pressure range, suggesting higher pressure and extended adsorption times are required. The adsorption isotherms, including two- and three-parameter models, suggested that the adsorption process was likely dominated by a monolayer on a homogenous surface. Furthermore, the kinetic analysis using pseudo-first- and pseudo-second-order models demonstrated

ambiguous results due to incomplete adsorption. To address this, the Elovich model was applied, indicating the CO_2 adsorption by ZIF-76 involved a complicated mechanism. Overall, the findings highlight the potential of ZIF-76 as a promising adsorbent for CO_2 capture with further optimization needed to enhance adsorption efficiency and overcome kinetic limitations.

Supplementary Materials: The following supporting information can be downloaded at: https://www.mdpi.com/article/10.3390/pr13020320/s1, Table S1: Yield of ZIF-76; Figure S1: FTIR spectra of reactants; Figure S2: Various morphologies of ZIF-76_B, including (a) irregular cubic, (b) needle-like shape and (c) spherical; Figure S3: CO_2 adsorption-desorption isotherm for (a) ZIF-76_A and (b) ZIF-76_B at 298.15 K

Author Contributions: Conceptualization, N.M.Y., M.A.B., K.J. and E.A.; methodology, N.M.Y. and S.F.N.A.A.; formal analysis, N.F.H. and A.H.A.R.; investigation, N.F.H.; resources, S.F.N.A.A.; data curation, N.F.H. and A.H.A.R.; writing—original draft preparation, N.F.H. and A.H.A.R.; writing—review and editing, N.M.Y.; supervision, N.M.Y.; project administration, N.M.Y.; funding acquisition, N.M.Y. All authors have read and agreed to the published version of the manuscript.

Funding: This research was funded by the Yayasan Universiti Teknologi PETRONAS-Fundamental Research Grant (YUTP-FRG) with the grant cost center (015LC0-436) under a research project entitled Functionalized Ionic Liquids-MOF Hybrid System for CO_2 Capture and the APC was also funded by 015LC0-436.

Data Availability Statement: The original contributions presented in this study are included in the article/Supplementary Materials. Further inquiries can be directed to the corresponding author.

Acknowledgments: The authors would like to acknowledge the Yayasan Universiti Teknologi PETRONAS (YUTP), for providing financial assistance under YUTP-FRG (015LC0-436), Universiti Teknologi PETRONAS and Centre for Research in Ionic Liquid (CORIL) for providing the required facilities to conduct this research work.

Conflicts of Interest: The authors declare no conflicts of interest.

References

1. Mondal, S.S.; Hovestadt, M.; Dey, S.; Paula, C.; Glomb, S.; Kelling, A.; Schilde, U.; Janiak, C.; Hartmann, M.; Holdt, H.-J. Synthesis of a partially fluorinated ZIF-8 analog for ethane/ethene separation. *CrystEngComm* **2017**, *19*, 5882–5891. [CrossRef]
2. Tranchemontagne, D.J.; Mendoza-Cortés, J.L.; O'keeffe, M.; Yaghi, O.M. Secondary building units, nets and bonding in the chemistry of metal–organic frameworks. *Chem. Soc. Rev.* **2009**, *38*, 1257–1283. [CrossRef]
3. Duan, C.; Yu, Y.; Hu, H. Recent progress on synthesis of ZIF-67-based materials and their application to heterogeneous catalysis. *Green Energy Environ.* **2022**, *7*, 3–15. [CrossRef]
4. Paul, A.; Banga, I.K.; Muthukumar, S.; Prasad, S. Engineering the ZIF-8 pore for electrochemical sensor applications—A mini review. *ACS Omega* **2022**, *7*, 26993–27003. [CrossRef]
5. Kalauni, K.; Vedrtnam, A.; Wdowin, M.; Chaturvedi, S. ZIF for CO_2 Capture: Structure, Mechanism, Optimization, and Modeling. *Processes* **2022**, *10*, 2689. [CrossRef]
6. Lai, Z. Development of ZIF-8 membranes: Opportunities and challenges for commercial applications. *Curr. Opin. Chem. Eng.* **2018**, *20*, 78–85. [CrossRef]
7. Ferreira, T.J.; de Moura, B.A.; Esteves, L.M.; Reis, P.M.; Esperança, J.M.; Esteves, I.A. Biocompatible ammonium-based ionic liquids/ZIF-8 composites for CO_2/CH_4 and CO_2/N_2 separations. *Sustain. Mater. Technol.* **2023**, *35*, e00558. [CrossRef]
8. Jones, C.G.; Stavila, V.; Conroy, M.A.; Feng, P.; Slaughter, B.V.; Ashley, C.E.; Allendorf, M.D. Versatile synthesis and fluorescent labeling of ZIF-90 nanoparticles for biomedical applications. *ACS Appl. Mater. Interfaces* **2016**, *8*, 7623–7630. [CrossRef] [PubMed]
9. Åhlén, M.; Jaworski, A.; Strømme, M.; Cheung, O. Selective adsorption of CO_2 and SF_6 on mixed-linker ZIF-7–8s: The effect of linker substitution on uptake capacity and kinetics. *Chem. Eng. J.* **2021**, *422*, 130117. [CrossRef]
10. Cubillas, P.; Anderson, M.W.; Attfield, M.P. Materials discovery and crystal growth of zeolite A type zeolitic–imidazolate frameworks revealed by atomic force microscopy. *Chem.–Eur. J.* **2013**, *19*, 8236–8243. [CrossRef] [PubMed]
11. Altarawneh, S.; Behera, S.; Jena, P.; El-Kaderi, H.M. New insights into carbon dioxide interactions with benzimidazole-linked polymers. *Chem. Commun.* **2014**, *50*, 3571–3574. [CrossRef]

12. Peralta, D.; Chaplais, G.; Simon-Masseron, A.; Barthelet, K.; Pirngruber, G.D. Synthesis and adsorption properties of ZIF-76 isomorphs. *Microporous Mesoporous Mater.* **2012**, *153*, 1–7. [CrossRef]
13. Hamidon, N.F.; Tahir, M.I.M.; Latif, M.A.M.; Abdul Rahman, M.B. Effect of altering linker ratio on nano-ZIF-8 polymorphisms in water-based and modulator-free synthesis. *J. Coord. Chem.* **2022**, *75*, 1180–1192. [CrossRef]
14. Lo, Y.; Lam, C.H.; Chang, C.-W.; Yang, A.-C.; Kang, D.-Y. Polymorphism/pseudopolymorphism of metal–organic frameworks composed of zinc (II) and 2-methylimidazole: Synthesis, stability, and application in gas storage. *RSC Adv.* **2016**, *6*, 89148–89156. [CrossRef]
15. Deneff, J.I.; Butler, K.S.; Reyes, R.A.; Sava Gallis, D.F. Harnessing Particle Size-Control and DNA-Oligo Functionalization in ZIF-76 for Biological Applications. *Adv. Mater. Interfaces* **2023**, *10*, 2201532. [CrossRef]
16. Jiang, D.; Huang, C.; Zhu, J.; Wang, P.; Liu, Z.; Fang, D. Classification and role of modulators on crystal engineering of metal organic frameworks (MOFs). *Coord. Chem. Rev.* **2021**, *444*, 214064. [CrossRef]
17. Bumstead, A.M.; Gómez, M.L.R.; Thorne, M.F.; Sapnik, A.F.; Longley, L.; Tuffnell, J.M.; Keeble, D.S.; Keen, D.A.; Bennett, T.D. Investigating the melting behaviour of polymorphic zeolitic imidazolate frameworks. *CrystEngComm* **2020**, *22*, 3627–3637. [CrossRef]
18. Chang, S.-S.; Clair, B.; Ruelle, J.; Beauchêne, J.; Di Renzo, F.; Quignard, F.; Zhao, G.-J.; Yamamoto, H.; Gril, J. Mesoporosity as a new parameter for understanding tension stress generation in trees. *J. Exp. Bot.* **2009**, *60*, 3023–3030. [CrossRef]
19. Qiu, X.; Yang, H.; Dejam, M.; Tan, S.P.; Adidharma, H. Experiments on the capillary condensation/evaporation hysteresis of pure fluids and binary mixtures in cylindrical nanopores. *J. Phys. Chem. C* **2021**, *125*, 5802–5815. [CrossRef]
20. Xiang, W.; Zhang, Y.; Chen, Y.; Liu, C.-j.; Tu, X. Synthesis, characterization and application of defective metal–organic frameworks: Current status and perspectives. *J. Mater. Chem. A* **2020**, *8*, 21526–21546. [CrossRef]
21. McEwen, J.; Hayman, J.-D.; Yazaydin, A.O. A comparative study of CO_2, CH_4 and N_2 adsorption in ZIF-8, Zeolite-13X and BPL activated carbon. *Chem. Phys.* **2013**, *412*, 72–76. [CrossRef]
22. Gu, Y.-M.; Yuan, Y.-Y.; Qadir, S.; Yuan, Z.-S.; Zhao, S.-S.; Sun, T.-J.; Liu, X.-W.; Wang, S.-D. Mixed-Linker Metal-Organic frameworks for carbon and hydrocarbons capture under moist conditions. *Chem. Eng. J.* **2022**, *433*, 134447. [CrossRef]
23. Švegovec, M.; Škrjanc, A.; Krajnc, A.; Logar, N.a.Z. Green synthesis approaches toward preparation of ZIF-76 and its thermal behavior. *Cryst. Growth Des.* **2023**, *23*, 3754–3760. [CrossRef]
24. Fatima, S.S.; Borhan, A.; Ayoub, M.; Ghani, N.A. CO_2 Adsorption Performance on Surface-Functionalized Activated Carbon Impregnated with Pyrrolidinium-Based Ionic Liquid. *Processes* **2022**, *10*, 2372. [CrossRef]
25. Amrutha; Jeppu, G.; Girish, C.; Prabhu, B.; Mayer, K. Multi-component adsorption isotherms: Review and modeling studies. *Environ. Process.* **2023**, *10*, 38. [CrossRef]
26. Ullah, S.; Bustam, M.A.; Assiri, M.A.; Al-Sehemi, A.G.; Gonfa, G.; Mukhtar, A.; Kareem, F.A.A.; Ayoub, M.; Saqib, S.; Mellon, N.B. Synthesis and characterization of mesoporous MOF UMCM-1 for CO_2/CH_4 adsorption; an experimental, isotherm modeling and thermodynamic study. *Microporous Mesoporous Mater.* **2020**, *294*, 109844. [CrossRef]
27. Chiban, M.; Soudani, A.; Sinan, F.; Persin, M. Single, binary and multi-component adsorption of some anions and heavy metals on environmentally friendly Carpobrotus edulis plant. *Colloids Surf. B Biointerfaces* **2011**, *82*, 267–276. [CrossRef]
28. Rahangdale, D.; Kumar, A. Chitosan as a substrate for simultaneous surface imprinting of salicylic acid and cadmium. *Carbohydr. Polym.* **2018**, *202*, 334–344. [CrossRef]
29. Piccin, J.; Dotto, G.; Pinto, L. Adsorption isotherms and thermochemical data of FD&C Red n 40 binding by chitosan. *Braz. J. Chem. Eng.* **2011**, *28*, 295–304.
30. Wang, T.; Jiang, M.; Yu, X.; Niu, N.; Chen, L. Application of lignin adsorbent in wastewater Treatment: A review. *Sep. Purif. Technol.* **2022**, *302*, 122116. [CrossRef]
31. Inglezakis, V.J.; Poulopoulos, S.G.; Kazemian, H. Insights into the S-shaped sorption isotherms and their dimensionless forms. *Microporous Mesoporous Mater.* **2018**, *272*, 166–176. [CrossRef]

Disclaimer/Publisher's Note: The statements, opinions and data contained in all publications are solely those of the individual author(s) and contributor(s) and not of MDPI and/or the editor(s). MDPI and/or the editor(s) disclaim responsibility for any injury to people or property resulting from any ideas, methods, instructions or products referred to in the content.